Mechanics of Materials 206 (2025) 105334

Contents lists available at ScienceDirect

Mechanics of Materials

journal homepage: www.elsevier.com/locate/mechmat

Research paper

Evaluation of NiTi under low-amplitude cyclic loading by means of thermographic harmonic analysis

V. Pinto [a,b], R. Cappello [a], S. Di Leonardo [a,b], G. Catalanotti [c,d], G. Burriesci [a,b,e], G. Pitarresi [a,*]

[a] Università degli Studi di Palermo - Dipartimento di Ingegneria, Viale delle Scienze, 90128, Palermo, Italy
[b] Fondazione Ri.MED, Gruppo di Bioingegneria, Via Bandiera, 11, 90133, Palermo, Italy
[c] Universidade de Evora, Departamento de Engenharia Mecatrónica, Evora, Portugal
[d] Università degli Studi di Enna Kore, Dipartimento di Ingegneria e Architettura, Enna, Italy
[e] University College London, UCL Mechanical Engineering, Torrington Pl, London, WC1E 7JE, UK

ARTICLE INFO

Handling editor: J Molinari

Keywords:
Shape memory alloys (SMA)
Nitinol
Super-elastic behaviour
Thermomechanical coupling
Thermoelastic effect
Elastocaloric effect
Harmonic analysis
Fast fourier transform

ABSTRACT

Nitinol is a shape memory alloy exhibiting superelastic behaviour above a specific temperature. This property has allowed the design of a new breed of collapsible/expandable cardiovascular medical devices, which are generally characterised by high-risk classes. Therefore, it is crucial to gain a comprehensive understanding of the material behaviour under in-vivo operating conditions. These are typically characterised by large pre-straining and small strain amplitude cyclic loading (high-cycle fatigue). In the present study, nitinol strips are monitored by two full-field sensing techniques: digital image correlation (DIC) and infrared thermography (IRT). The latter in particular was used to sample temperature during small-strain amplitude sinusoidal loading at various mean strains. Results show that the analysis of the frequency domain content of the temperature signal can provide useful information to characterise the material under operating conditions. In particular, it is found that temperature modulation is mainly characterised by its *first* and *second harmonics*, i.e. the harmonics at the load frequency and at twice the load frequency. These are shown to be correlated to the local stress field, the actual material phase status and the phase transformation history. The proposed harmonic analysis can be performed in near-real-time, and has the potential to be a convenient and highly informative tool when monitoring nitinol devices under structural fatigue testing. The paper also discusses the nature of the load-induced temperature modulation, and the direct applicability of the thermoelastic effect theory to interpret the observed behaviour.

1. Introduction

The behaviour of Nickel-Titanium (NiTi) alloys is characterised by three unique features: the ability to recover a preset shape under heat input (shape-memory effect), the ability to recover large strains (of the order of 8–10 %) due to stress-induced phase transformations (pseudo-elasticity or superelastic effect), and the ability to heat and cool significantly under phase transition (elasto-caloric effect, eCE). These properties are exploited in several innovative devices in various engineering applications, including mechanical actuators, dampers, biomedical implants, solid state coolers, etc. (Tzamtzis et al., 2013; Zhu et al., 2024; Morgan, 2004; Tušek et al., 2018). This has also nourished a wealth of inter-sectorial and inter-disciplinary studies, mainly focused on multi-scale thermomechanical characterisations of the material, with the purpose of predicting, controlling and enhancing the aforementioned behaviours according to each application need.

In this paper, attention is focused on the superelastic behaviour of NiTi. This condition is of particular interest to the biomedical sector, as it has enabled the design of a special class of collapsible and self-expanding cardiovascular implants, including stents for angioplasty, endo-grafts, and trans-catheter heart valve frames (Wadood, 2016; Petrini and Migliavacca, 2011). As these components normally need to guarantee several million cycles of functional life (each year they experience an average of 40 million cardiac cycles), high-cycle fatigue failure is a risk that needs to be assessed and prevented (Mahtabi et al., 2015). More specifically, in-vivo fatigue loading for NiTi collapsible devices typically occurs after the material has undergone a “pre-strain” cycle, as the effect of the crimping phase is associated with the loading of

* Corresponding author.
E-mail address: giuseppe.pitarresi@unipa.it (G. Pitarresi).

https://doi.org/10.1016/j.mechmat.2025.105334
Received 17 July 2024; Received in revised form 13 February 2025; Accepted 20 March 2025
Available online 21 March 2025

the prosthesis in the delivery system. When implanted, the component experiences a partial self-expansion (Catoor et al., 2019; Pelton et al., 2022), which commonly leaves a non-homogeneous parent/martensite phase distribution at the mesoscale (Morgan, 2004; Bonsignore et al., 2019). Therefore, the pre-straining cycle involves a large deformation with stress-induced martensite transformation (SIMT) and a partial return to austenite, that can locally modify the material behaviour. A cyclic full or partial stress-induced phase transformation rapidly accumulates significant changes in the superelastic behaviour (*functional fatigue*), leading to early fatigue failure after relatively low cycle counts (Melton and Mercier, 1979). This functional fatigue (Xie et al., 2016; Soul and Yawny, 2017), is only partially developed for the conditions normally occurring in cardiovascular implants, where the full pseudo-elastic cycle is limited to the pre-straining stage. In fact, the cyclic nature of in-vivo operating loads is mostly associated with blood pressure fluctuations induced by the cardiac cycle, which determines a *high cycle structural fatigue* scenario characterised by small strain amplitudes around a non-null mean strain/stress, which may represent the natural cause of prosthesis final failure (Mitchell et al., 2019; Senthilnathan et al., 2019; Launey et al., 2023). The importance of reproducing a realistic testing scenario in the fatigue assessment is also recommended by FDA guidance (Technical Considerations for Non, 2021), which advises to setup tests in displacement control with a realistic preconditioning simulation, including pre-straining.

From the above, it then emerges the significance of characterising the material behaviour under small strain amplitude cyclic loading, starting from a mean strain enabling a hybrid mesoscopic parent/daughter phase distribution (mixed-phase state (Catoor et al., 2019)). Schlun et al. (2011) were among the first to recognise this as a more application-oriented material characterisation and performed fatigue tension-tension cycles in strain control on NiTi wires, starting from a mean strain along the lower plateau. They showed that below certain cyclic strain amplitude thresholds the material exhibited good functional stability and limited cycling hysteresis. More recently, Launey et al. (Pelton et al., 2022; Launey et al., 2023) performed similar tests, varying the mean strain value along the lower plateau, showing that cycling at higher mean strains determined a reduced average stress amplitude due to a smaller cyclic modulus, associated with the martensite smaller Young's moduli, and this led to an improved fatigue life.

A particularly useful testing configuration for investigating the cyclic behaviour of NiTi at the mesoscale is the dog bone or strip plate under tension-tension. In fact, the flat surface facilitates the implementation of full-field non-contact techniques such as Digital Image Correlation (DIC) and Infrared Thermography (IRT) (Delpueyo et al., 2011, 2021). Hence, this type of sample coupon has become popular to investigate the non-homogeneous nature of stress-induced phase transformations (Churchill et al., 2010; Kim and Daly, 2011; Reedlunn et al., 2013; Schlosser et al., 2009; Zheng et al., 2017).

DIC has been a particularly effective technique for monitoring localised SIMT and investigating transition zones between parent and daughter phases (Catoor et al., 2019; Zheng et al., 2016; Zhang and He, 2018; He, 2023). These generally take the form of Lüders bands with possible smaller branching bands, that have been identified as favourite sites of crack nucleation leading to fatigue failure. This is ultimately due to the onset of stress concentration sites (Zhang and He, 2018; He, 2023), geometry necking (Zhang and He, 2018), dissipation at microscopic inter-granular austenite/martensite interfaces (Zhang and He, 2018), and re-activation of localised cyclic SIMT inside the phase transition zones (Catoor et al., 2019; Zheng et al., 2017).

The use of infrared cameras and IRT has also recently emerged to investigate the behaviour of NiTi, often coupled with DIC (Delpueyo et al., 2021; Churchill et al., 2010; Schlosser et al., 2009; Pieczyska, 2010). A recent survey of works investigating SMAs using IRT, DIC and DIC + IRT, is provided in (Delpueyo et al., 2021). Most works have used IRT to monitor partial or full cyclic SIMT. The major outcomes have been mainly qualitative and comprise the ability to detect the localised or diffused latent heat sources or sinks of phase transformation and the correlation between the ongoing latent heat and modifications in transformation stresses due to their temperature sensitivity (Churchill et al., 2010; Pieczyska et al., 2013). IRT has also contributed to highlighting the thermomechanical correlations with deformation rates, since going from slow to faster strain rates coincides with an evolution from isothermal to adiabatic conditions, which can have a significant impact on the material response (Churchill et al., 2010; Pieczyska et al., 2013; Zhang et al., 2017).

Relatively few studies have investigated the temperature evolution during cyclic loading of NiTi, most of which with emphasis on functional fatigue (Tušek et al., 2018; Yin et al., 2021; Ahadi et al., 2018; Furgiuele et al., 2020). It is generally observed that temperature has a fluctuation whose modulation is correlated with the loading wave (Ahadi et al., 2018; Di Leonardo et al., 2021). It is therefore postulated that such modulation is induced by reversible thermomechanical heat sources. These are mostly associated with two main effects: the eCE, which considers the latent heat of phase transformation, and the thermoelastic effect (TE), which is caused by the elastic local volume change. The reversible nature of both effects may explain the peculiar temperature modulation when a loading waveform is applied. In the high-cycle fatigue scenario analysed in this paper, cyclic SIMT is not activated, and this should play out the contribution of the eCE heat source, leaving TE as the main thermomechanical coupling responsible for temperature modulation. Based on this assumption, Eaton-Evans et al. (Dulieu-Barton et al., 2007; Eaton-Evans et al., 2006) have analysed the thermoelastic signal, i.e. the temperature harmonic at the loading frequency, when the load is applied as a sinusoidal wave. The authors observed that, unlike common materials, the thermoelastic signal measured with NiTi alloys is in phase with the loading sine wave (i.e. the material heats up when loaded in tension). This behaviour was justified in (Dulieu-Barton et al., 2007; Eaton-Evans et al., 2006) by recalling the Second-Order Thermoelastic Theory (Wong et al., 1987, 1988). More recently, Di Leonardo et al. (Di Leonardo et al., 2021) have investigated the whole harmonic content of temperature on a NiTi strip under low strain amplitude loading, applying a triangular wave load modulation at 2 Hz. They observed that the temperature signal has a similar triangular wave modulation and showed a significant second harmonic, i.e. the harmonic at twice the main loading frequency.

The main aim of the present work is to investigate the features of the temperature harmonic content when a NiTi strip is subject to sinusoidal cyclic loading typical of in-vivo working conditions. This is with the purpose of identifying and exploiting potential qualitative and quantitative correlations between the temperature harmonics and the status of the material. To do so, NiTi strips have been tested by first conducting quasistatic traction tests monitored with DIC and IRT, and then applying small amplitude sinusoidal loading and analysing the frequency domain content of the temperature acquired by IRT. Several advances have been presented over past similar thermomechanical studies. Compared to (Dulieu-Barton et al., 2007; Eaton-Evans et al., 2006), a flat strip sample is considered, allowing to better investigate the influence of Lüders bands propagation and austenite/martensite interfaces. Furthermore, the second harmonic of temperature is also evaluated, allowing a more in-depth comparison between the NiTi behaviour and the predictions of the thermoelastic effect higher-order models. Compared to (Di Leonardo et al., 2021), the present work implements a pure sinusoidal loading, allowing a more controlled phase synchronisation between the load and temperature signal and the adoption of coherent sampling to reduce spectral leakage in the analysis of the frequency content (Pitarresi et al., 2020). Another advance over (Di Leonardo et al., 2021; Wong et al., 1987) is also the analysis of the material response under a wider and more controlled number of statuses including virgin austenite, retransformed austenite and martensite.

2. Materials and methods

2.1. Sample preparation and plan of experiments

Two rectangular NiTi alloy strips were tested, with 0.4 mm thickness, 6 mm width and 100 mm length. Both samples were cut from the same plate (56 % Ni, 44 % Ti) by electrical discharge machining, to minimise the introduction of residual stresses and heat-affected zones along the cutting regions. The two samples are hereinafter denominated as S1 and S2. Both samples were tested at room temperature.

Sample S1 was tested under quasistatic tension, monitoring the full pseudo-elastic cycle with DIC. The test was performed in an electro-mechanic Instron 3367 testing machine, in displacement control at 0.5 mm/min (corresponding to 10^{-4} s^{-1} nominal axial strain rate), up to a nominal strain value of about 8 %, and successively unloaded at the same speed, down to 0 N. The analysed surface was prepared for DIC by applying a matt-white uniform paint and a matt-black speckle, using an airbrush gun connected to an air drier compressor.

Sample S2 was tested in an Instron Electropulse E10000 electrodynamic testing machine, with a distance between the upper and lower gripped areas of 50 mm. Two tests were performed in succession, which are here described.

- Test S21: sequence of loading/unloading monotonic ramps at a constant crosshead displacement rate of 0.5 mm/min, up to a maximum displacement of 2.9 mm, corresponding to a maximum average axial strain of about 5.8 % (see Fig. 1). Each ramp is set to start and finish at a 0 N force.
- Test S22: single cycle up to a maximum nominal axial strain of 6.6 %, with four cycling windows. Start and finish values of each stage (ramp, or cycle) are reported in Fig. 2 (see the plot legend). Ramps applied a quasi-static load in displacement control at 0.5 mm/min. Cycles consisted of sinusoidal loading under displacement control, with a peak-to-peak amplitude of 0.3 mm that corresponds to a nominal peak-to-peak average axial strain of 0.6 %. The cycling frequency was 3 Hz, and the cycling window had a duration of 150 Section Fig. 2 summarises the nominal stress-strain curve, with the four cyclic windows indicated with different colours. The four cyclic windows are positioned at different mean strain levels. *Cycle 1* (curve in red) is positioned about halfway between zero stress and the upper plateau stress.

Cycle 2 (curve in black) and *Cycle 3* (curve in green) start at two different strain levels from the upper plateau, 3.4 % and 6.6 %, respectively. Finally, *Cycle 4* (curve in magenta) starts at the strain of 3.4 % from the lower plateau.

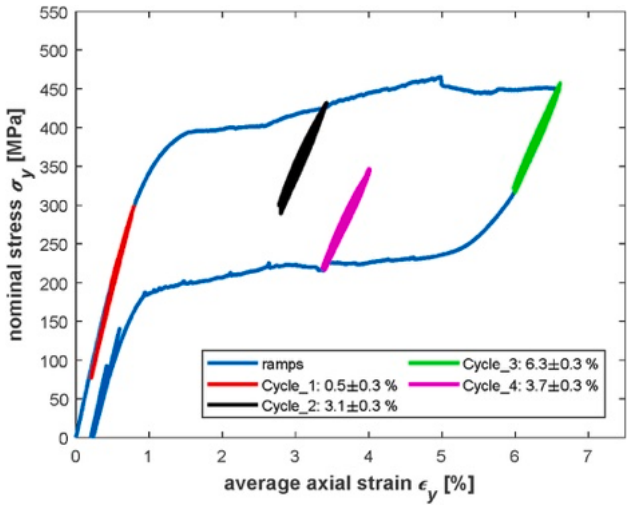

Fig. 2. Mixed quasi-static + cyclic tensile test S22: loading ramps in blue and cycling windows in red (austenitic phase), black and green (from upper plateau) and magenta (from lower plateau). (For interpretation of the references to colour in this figure legend, the reader is referred to the Web version of this article.)

Cycle 2 was intentionally run from a lower deformation than the one reached in test S21 (3.4 % against 5.8 %), so that a transformation front could be observed between martensite and non-virgin austenite, i.e. re-transformed austenite. The transformation front then progressed up to about 6.7 % (i.e. beyond 5.8 %) so that *Cycle 3* comprised a transformation front between martensite and virgin austenite.

Cycle 1 was instead run before the onset of SIMT, i.e. within the fully austenitic region, but still the sample presented a non-homogeneous mesoscale status, with the upper half of the sample which is made of re-transformed austenite, and the lower half of predominantly virgin austenite.

Both tests S21 and S22 were monitored with IRT, and in order to enhance and uniform the emissivity in the infrared spectrum, the sample surface stared by the IR camera was painted with a uniform matt-black acrylic paint.

2.2. DSC analysis

The Differential Scanning Calorimetry (DSC) sample, consisting of a chip of weight equal to 38.6 mg, was extracted from the NiTi alloy plate

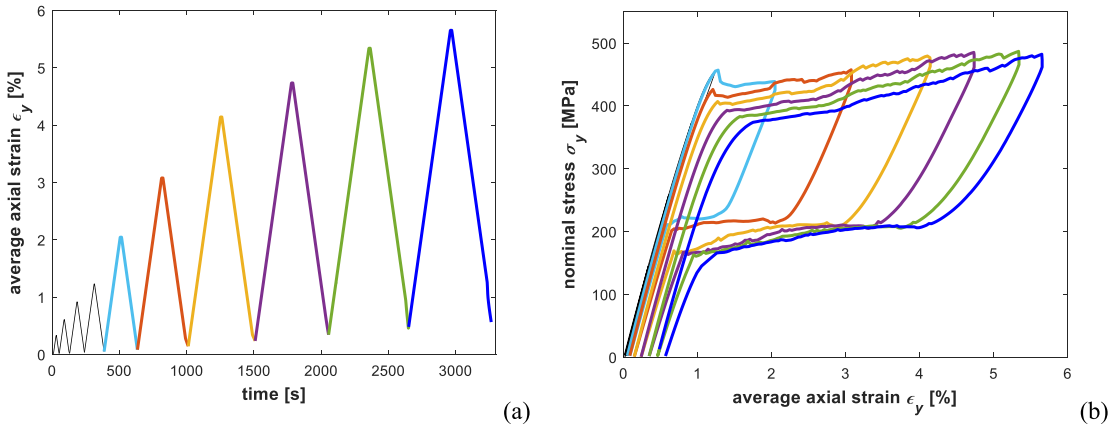

Fig. 1. Preliminary cyclic SIMT test S21. a) sequence of monotonic quasistatic loading/unloading ramps in displacement control at 0.5 mm/min (0.0017 s^{-1} strain rate); b) average strain versus nominal stress curves corresponding to loading ramps.

and used to perform a DSC analysis. DSC was performed to evaluate the phase transformation temperatures. A Setaram DSC131 system (Caluire-et-Cuire, France) was used, setting a sequence of cooling and heating ramps from −40 °C to 200 °C at a constant rate of 10 °C/min. Analysing the heat flow versus temperature allowed to identify the peak, start and end temperatures of phase transformations (M_p, A_p, M_s, M_s, M_f and A_f) as described in ASTM F2004 (ASTM F2004-17, 2017). Results are analysed in Section 3.1.

2.3. DIC experimental setup

During test S1, a Nikon reflex D5100, equipped with a macro lens Micro-Nikkor 105 mm f/2.8, was used to capture images at intervals of 5 s. Image capture was remotely controlled via a PC by the software DigiCamControl (DigiCamControl web site, 2024). The images were then post-processed with the Matlab-based NCORR software (Blaber et al., 2015), where the following parameters were set for the analysis: subset radius 10 px, subset spacing 5 px and strain radius (equivalent to the virtual strain gauge) of 3 subset-spacings. The processed images presented a magnification factor of 0.03 mm/px.

2.4. IRT experimental setup

An infrared camera Flir X6540sc was used to acquire thermograms throughout tests S21 and S22. During cyclic loading, the cooled sensor integration time was set to 659 μs. This allowed a frame rate of 200 Hz, which is sufficiently high to allow an accurate harmonic analysis of the temperature signal.

The thermograms field of view also included the aligning brackets used to align the specimen in the load direction of the testing machine (see Fig. 3a). These are rigidly connected to the grips, with the upper bracket connected to the moving grip. Two regions of interest (ROIs), used to analyse their average temperature, were selected on the upper and lower part of the specimen, identified as ROI UP and ROI DW. The ROI DW, in particular, was confined inside the zone of the sample which remains as virgin austenite during all four cyclic windows, while ROI UP laid on the transformed austenite in *Cycle 1* and on martensite in *Cycle 2*, *3*, *4*. Since the bracket exhibits a significantly higher emission than the background, a further region of interest (identified as ROI Load) was selected across the background and the bracket, so that the average temperature could reproduce the displacement signal and hence the loading signal (edge-modulation effect (Boyce and Lesniak, 2019)).

The average signals from the previous ROIs were synchronised to allow the analysis of the phase of the temperature harmonics with respect to the applied load phase (see Section 3.4).

2.4.1. IRT signal post-processing

The sequence of acquired thermograms was processed in MATLAB, where data could be easily imported by using the FLIR Science File SDK transfer tool. One aim of the signal analysis was to extract the amplitude and phase maps of the first harmonic (i.e. the harmonic at the load frequency of 3 Hz) and of the second harmonic (6 Hz) during cyclic loading. This was accomplished by implementing two alternative in-house developed scripts, one based on the *discrete Fourier transform* (DFT) and one on the *least-square fitting* (LSF).

The DFT was applied to 3000 frames, corresponding to 15 load cycles and 5 s of sampling. This choice allowed to fulfil the coherent sampling requirement and avoid the occurrence of spectral leakage (Pitarresi et al., 2020), placing bins at 3 and 6 Hz in the frequency domain axis. The analysed periods were taken at the end of the cycling interval, which lasted 50 s. This allowed the average temperature to become more steady and uniform, since previous localised phase transformation and loading cycles determine an initial temperature non-uniformity. An example is evidenced in Fig. 3c, where the average temperatures in ROI UP and ROI DW are different when the load starts cycling.

In selecting the time window for data processing, the initial time was taken to coincide with a peak of the average ROI Load signal. Therefore, the load signal ω harmonic is represented as a cosine wave. Since the Matlab *fast Fourier transform fft* function implements a decomposition into cosine harmonics, this allows to obtain a zero phase at the 3 Hz harmonic for the ROI load signal. With this time basis reference, the phase values of the 3 Hz harmonic of the temperature will represent the shift of temperature with respect to the loading wave.

The LSF data processing, on the other hand, consisted of fitting data

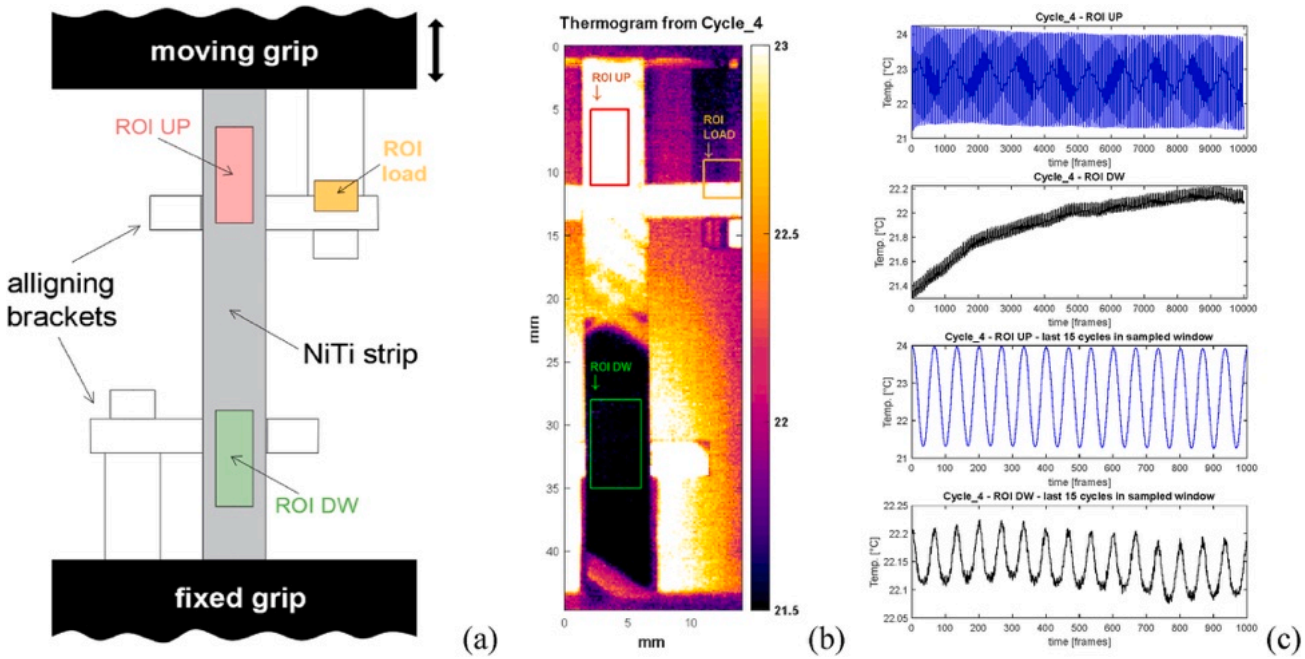

Fig. 3. a) position of ROIs in a schematic drawing of the gripped sample with aligned brackets; b) position of ROIs in a thermogram from *Cycle 4*; c) plots of average temperatures from ROI UP and DW *versus* time expressed in number of frames, during *Cycle 4*.

with an analytical model with three harmonic terms defined as follows (Cappello et al., 2022):

$$T(t) = T_o + B \cdot t + F\cos(\omega \cdot t + \phi_T) + S\cos(2\omega \cdot t + \phi_S) + R\cos(3\omega \cdot t + \phi_R) \quad (1)$$

where T_o and B account for an average and a linear temperature increase, F, S, R and ϕ_F, ϕ_S, ϕ_R are the amplitudes and phases of three harmonic terms at ω, 2ω and 3ω (where $\omega = 2\pi f$ and f corresponds to the loading frequency, i.e. 3 Hz in this work). It is noticed that a cosine representation is also used, to allow a direct comparison with the DFT results. A linear term is also introduced to better consider residual average temperature gradients. It is here anticipated that the amplitude and phase maps of the harmonics obtained by the DFT and LSF were practically identical, thus providing a validation of the whole data processing scheme. In the following, the first and second harmonic amplitudes will be indicated with F and S, and the respective phases with *phF* and *phS*.

2.5. Thermomechanical model evaluation

The temperature modulation observed during cyclic loading was also analysed to establish whether and to what extent it agrees with the TE theory (Pitarresi and Patterson, 2003). In general, the thermomechanical behaviour of solid matter can be modelled via the heat conduction equation written in the form of a power balance as (Lemaitre et al., 1993):

$$\rho C_\varepsilon \dot{T} - k\nabla^2 T = D + T\frac{\partial \sigma_{ij}}{\partial T}\dot{\varepsilon}_{ij} + T\rho\frac{\partial^2 H}{\partial T \partial \mathbf{x}}\dot{\mathbf{x}} + q_s \quad (2)$$

where ρ is the density, C_ε the specific heat at constant volume, and k is the isotropic thermal conductivity. Terms on the right-hand side describe heat sources, where D is the heat from energy dissipation, the second term describes the thermo-mechanical coupling associated with the TE (Pitarresi and Patterson, 2003), the third term accounts for the thermo-mechanical coupling associated with changes in the internal state of matter (Lemaitre et al., 1993; Chrysochoos et al., 2010; Peyroux et al., 1998), and finally accounts for external heat sources.

It is reasonable to assume that under low strain amplitude cyclic loading (as established under high-cycle fatigue), the material is not damaging and behaves as linear elastic. In the absence of significant external heat sources, and if the sample is in thermal equilibrium and the reversible temperature changes arise under nearly adiabatic conditions (this is an acceptable condition above a certain loading frequency), then Eq. (2) can be simplified into:

$$\rho C_\varepsilon \frac{\dot{T}}{T} = \frac{\partial \sigma_{ij}}{\partial T}\dot{\varepsilon}_{ij} \quad (3)$$

By neglecting the dependency of the elastic Hooke's parameters from T, the well-known first-order thermoelastic law (FOTL) can be obtained as (Pitarresi and Patterson, 2003):

$$dT = -T_o\frac{\alpha}{\rho C_p}d\sigma_{kk} \quad (4)$$

where σ_{kk} represents the first stress invariant. Wong et al. (1987) also included the dependence of the elastic parameters on temperature, thus obtaining a formulation known as the second-order thermoelastic law (SOTL).

In the present work, the thermal response of NiTi is investigated under a nominally linear elastic regime and uniaxial tensile tension, where tension modulation due to cyclic loading can be assumed as a mono-frequency harmonic law such as: $\sigma_m + \sigma_a(\sin\omega t)$, where σ_m and σ_a are mean and amplitude axial stress components. The FOTL and SOTL for this case can be written as (Di Leonardo et al., 2021; Wong et al., 1987):

$$\dot{T} = -T_o K_o \sigma_a \sin(\omega t) \quad (5)$$

$$\dot{T} = -T_o K_\omega \sigma_a \sin(\omega t) - T_o K_{2\omega}\sigma_a^2 \cos(2\omega t) \quad (6)$$

where the thermoelastic coefficients K_o, K_ω and $K_{2\omega}$ are (Peyroux et al., 1998):

$$K_o = \frac{\alpha_o}{\rho C_p}; \quad K_\omega = \frac{1}{\rho C_\varepsilon}\left[\alpha - \frac{1}{E^2}\frac{\partial E}{\partial T}\sigma_m\right]; \quad K_{2\omega} = \frac{1}{\rho C_\varepsilon}\left[\frac{1}{4E^2}\frac{\partial E}{\partial T}\right] \quad (7)$$

The physical parameters involved in the above thermoelastic coefficients and the absolute temperature T_o are all positively defined, therefore, the temperature first harmonic according to the FOTL (Eq. (5)) varies in the opposite phase to the loading wave. The SOTL, on the other hand, can predict cases where the first harmonic of temperature is in phase with the load. This is possible when K_ω is negative, which requires that $\partial E/\partial T$ is positive and greater than $E^2\alpha/\sigma_m$ (Eaton-Evans et al., 2006; Dulieu-Barton et al., 2008).

The SOTL predicts also a second harmonic wave in response to a mono-frequency load. A positive $\partial E/\partial T$ implies that this second harmonic of temperature is modulated as -cos(2ωt). Previous work on NiTi focused only on the first harmonic response (Eaton-Evans et al., 2006; Dulieu-Barton et al., 2008), noting how the austenite and martensite responses were both in phase with the loading wave, and therefore suggesting that the behaviour followed the SOTL in the case when the first harmonic coefficient K_ω is negative. This condition is also schematically represented in Fig. 4, where the amplitudes of the first and second harmonics are normalised to 1, whereas the phases are modulated according to sin(ωt) (blue curve) and -cos(2ωt) (red curve).

3. Results and discussion

This section presents and comments on the principal results from the DSC, DIC and IRT analyses, with section 3.5 reporting a final general discussion on the observed thermomechanical behaviour during low strain amplitude cycling.

3.1. DSC results

Fig. 5 reports the measured heat flow versus temperature curve. The presence of a single exothermic peak and a single endothermic peak, indicate that the material does not exhibit an intermediate R-phase transformation. The start, peak and finish phase transformation temperatures resulted equal to $M_s = 8.3$ °C, $M_p = -4.4$ °C and $M_f = -18.7$ °C, and $A_s = -17.1$ °C, $A_p = -5.2$ °C and $A_f = 5.2$ °C, respectively. Therefore, the DSC analysis confirmed that the austenite phase is stable at room temperature and the material is expected to exhibit a superelastic behaviour.

3.2. DIC results

Fig. 6 shows a nominal stress versus average strain curve measured on a virgin sample S1. The points marked along the curve indicate the positions where maps of the axial strain ε_{yy} from DIC are evaluated, as

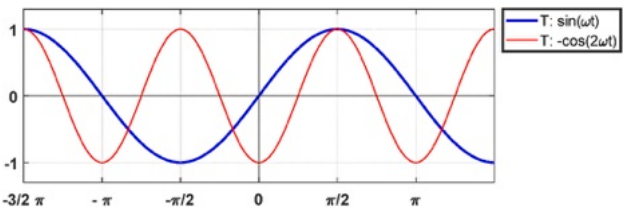

Fig. 4. Schematic representation of the first and second harmonics phases of the temperature signal according to the SOTL when $\partial E/\partial T > E^2\alpha/\sigma_m$.

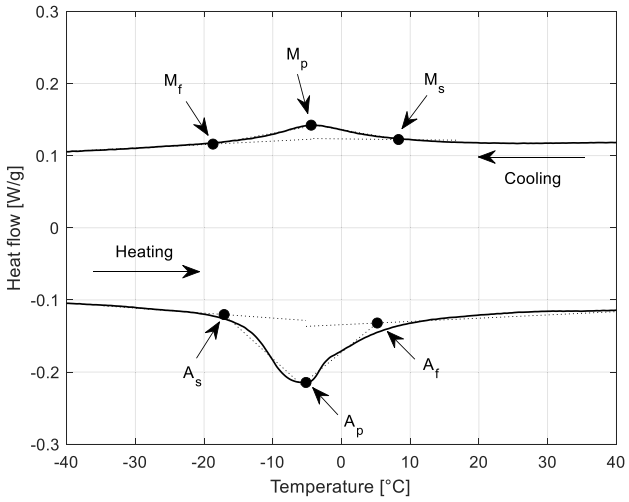

Fig. 5. DSC heat flow curve.

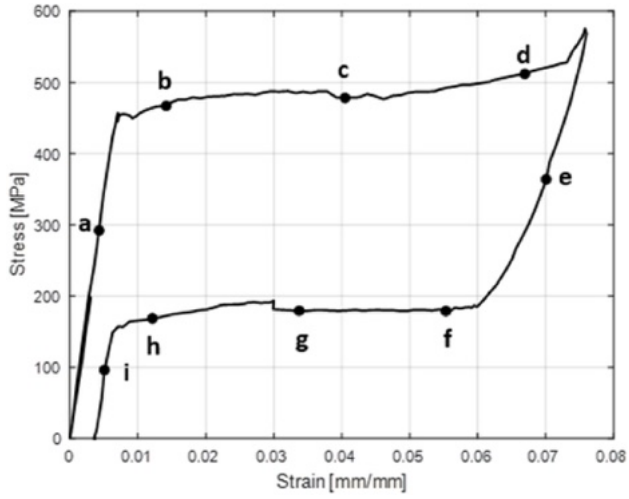

Fig. 6. Nominal stress-strain curve obtained from test S1.

reported in Fig. 7. Each strain map is accompanied by a binary representation of the strain, where the martensitic region is represented in dark grey and the austenite in light grey. These binary maps are obtained after amplifying the horizontal displacement by a tenfold factor. This allows to emphasise the presence of lateral displacements due to spurious bending arising during the tensile test, whose origin is explained in (Di Leonardo et al., 2022). The ability of DIC to detect SIMT and map the austenitic and martensitic regions is well documented in the literature, as recalled in the Introduction section. It is interesting here to point out that the sample exhibits a highly localised phase transformation, at least when no repeated SIMT and functional fatigue have occurred yet. Focusing on transformation fronts, it is observed that these follow two different shapes: a straight front that obliquely crosses the whole sample width, and a fishbone-like front, where a transformation band is mirrored around the sample axis by another band or multiple spike-like bands. This pattern can be related to the aspect ratio of the sample, recognised as a parameter that can affect the nucleation of transformation bands (Xiao and Jiang, 2022).

The amplified grey-scale representation provides a suggestion to understand the mechanism that determines the observed transformation front shapes. In fact, a single straight front generates a significant lateral displacement. This happens to accommodate the fact that the left and right sides of the sample have different elongations, which the sample fixed grip and the slow crosshead displacement cannot compensate. The rise of an in-plane bending increases the stored strain energy. Therefore, the evolution of new transformation fronts, as well as the single front progression, will evolve, according to the attempt to reduce such mechanical energy. This explains why multiple straight fronts are generally all parallel (as shown also in Fig. 7 d–f, g, h). In this case, two parallel fronts produce two counter-rotations which reduce the flexural bending. Another mechanism of front propagation is the straight front mirroring, i.e. the formation of a fishbone-like morphology (see Fig. 7 b, c, g).

3.3. Test S21: quasistatic pre-conditioning

Fig. 1b reports the nominal stress-strain curves measured during the load-unload cycles shown in Fig. 1a. It is worth observing that the material presents several typical features of NiTi functional fatigue. Each repeated forward transformation (austenite-to-martensite) is activated at progressively lower stresses, while the original stress level is again reached when the transformation involves a virgin austenite zone. Also, the upper plateau shows a slight increasing slope that can be related to a general temperature increase caused by the forward transformation, which raises the transformation stress. The lower plateau stress gets lower with repeated transformations but at a smaller rate than the upper plateau stress. The decreasing slope of the lower plateau is again justifiable with an overall temperature decrease arising with the progression of the reverse transformation (martensite-to-austenite). Finally, it is observed a progressive accumulation of residual deformation after each cycle, which is in part due to the slipping of the sample from the grips, and in part due to residual plastic deformation (residual martensite).

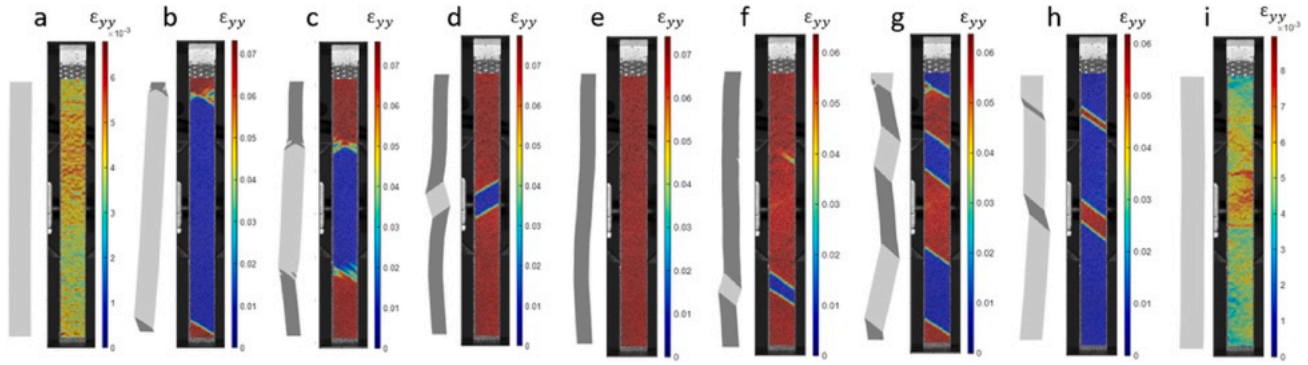

Fig. 7. Maps of the axial strain ε_{yy} at various stages of loading (see Fig. 6). Next to each strain map is reported a representation of the sample with the distribution of austenitic (light grey) and martensitic (dark grey) zones and amplified transverse ε_{xx} deformation.

3.4. Test S22: quasistatic + cyclic loading

Fig. 2 reports the position of the cyclic loading windows during the quasistatic cycle. The localised heating/cooling occurring at the formation of Lüders bands during quasistatic loading was readily detected by the IR camera. This allowed the tracking of the transformation front separating austenite and martensite, and then schematically mapping the sample phase status present during the four cycling windows. A schematic representation is represented in Fig. 8, which will help to comment on the harmonics features presented in the next sections. Areas in white in Fig. 8 indicate regions where the material is preserved in its virgin austenitic phase status. Areas reported in a shed of grey represent zones of retransformed austenite, i.e. austenite recovered from one or more previous phase transformations between austenite and martensite. A darker shade of grey indicates a higher number of back and forward phase transformations. This is, for instance, the case of the upper part of sample S2 during cyclic window 1 in test S21, where the sample has already undergone six transformations corresponding to the coloured triangular cycles in Fig. 1a. Finally, areas reported in blue indicate a martensitic status.

It is here reported also that, during the cyclic loading, the phase transformation fronts did not progress and remained in the position reached just before the cycling start. Another noteworthy feature is that the four cyclic stages did not show significant hysteresis. This can also be appreciated from Fig. 2 and can be interpreted as a further sign that no cyclic SIMT is present during the fatigue loading.

In the following subsections, Figs. 9, 11, 13 and 14 report the maps of the first and second harmonic, both in amplitude and phase, obtained from each cyclic window.

3.4.1. S22: Cycle 1

As shown in Fig. 9, the amplitude maps of both the first and second harmonic (*F* and *S*) show a higher signal in the upper half of the sample, i.e. where the material presents a non-virgin austenite. It is observed also that the signal increases towards the top end of the sample, i.e. the material produces a higher temperature amplitude at both ω and 2ω, with an increasing number of previous phase-transformations, i.e. with the accumulation of functional fatigue. It is also observed that the amount of temperature change in the plural-retransformed austenite becomes a few tenths of a degree. This is a rather high value if compared to typical thermoelastic signals from metallic materials at similar levels of stress amplitudes (Cappello et al., 2022).

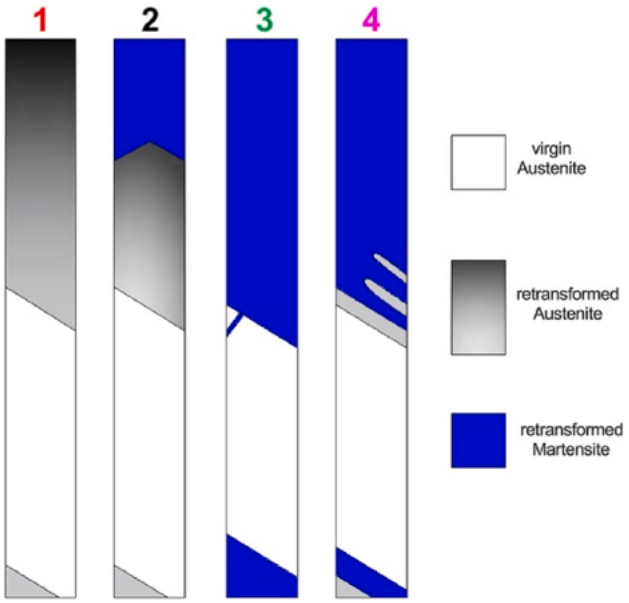

Fig. 8. Schematic map of material phase status at each of the four cycling windows.

The phase map of the first harmonic (*phF*) shows a rather peculiar phase jump of about 180° between the virgin austenite and the retransformed austenite. The second harmonic phase (*phS*) is instead uniform over the whole surface. As mentioned in Section 2.4, the time window analysed is initiated at a peak value of the loading wave, which is then represented as a cosine wave. Since the Matlab *fft* is also decomposing signal harmonics as cosine waves with reference to sampling initiation, a value of zero in *phF* means that the first harmonic is in phase with the load. In the present case, the retransformed austenite is in phase with the load, while the virgin austenite zone is in the opposite phase. To further investigate this peculiar outcome, Fig. 10 reports the average temperature acquired from ROI Load, ROI UP and ROI DW. While the load signal is well-fitted by a cosine waveform, the temperature response seems to invert its sinusoidal trend whenever the load decreases under a certain value. This is highlighted in Fig. 10 by comparing the waveforms inside the two straight vertical bars. Moreover, Fig. 10 shows that the part of the temperature waveform that is in phase with the load waveform has a much higher amplitude in the retransformed austenite (ROI UP) than in the virgin austenite (ROI DW). This is the reason why the retransformed austenite produces a first harmonic where the prevailing phase is aligned with the load waveform, while the first harmonic of the virgin austenite sees a prevailing phase opposite to that of the load. For each temperature profile in Fig. 10 (first column) the power spectrum is reported aside (Fig. 10, second column). It is seen that the main peaks at ω and 2ω (i.e. 3 and 6 Hz) present low spectral leakage. Moreover, the second harmonic amplitude is rather high, and even higher than the first harmonic amplitude for the signal relative to ROI DW. Similar results have been reported in (Pinto et al., 2024), where the peculiar thermomechanical behaviour of the austenitic NiTi is further investigated by applying different loading amplitudes.

Temperature power spectra in Fig. 10 report that harmonics beyond 2ω consistently exhibit negligible amplitudes, typically below 0.005 K, slightly higher than the noise floor. This observation consistently holds across all other loading cycles (*Cycles 2, 3, 4*).

It can be concluded also that the second harmonic of the temperature waveforms shown in Fig. 10 is modulated as $-\cos(2\omega)$, i.e. the same modulation predicted by the SOTL in Eq. (6) and in Fig. 4. This could be regarded as a confirmation that this thermomechanical model is valid for the actual material status.

3.4.2. S22: Cycle 2

During *Cycle 2* the upper part of the sample has transformed from austenite to martensite. All the harmonic maps are reported in Fig. 11, showing features that can be correlated to the material status.

It is first observed that the *F* value is still lower in the virgin austenitic region and higher in both retransformed austenitic and martensitic regions. Compared to *Cycle 1*, the values of *F* have increased quite significantly, even if the load cycle is oscillating with the same peak-to-peak displacement range. Now the temperature changes of the ω harmonic are as high as a few degrees. Recalling K_ω from Eq. (7), it is seen that temperature amplitude is expected to increase linearly with the applied mean stress, but the increase from about 200 MPa in *Cycle 1* to about 350 MPa in *Cycle 2* is less than twofold, while the observed increase of *F* is much higher. The circumstance that the material in *Cycle 2* is stressed near the margin of a SIMT might increase the extent of local volume change and thus the thermoelastic effect. Interestingly, it is observed that the zones where *F* reaches peak values coincide with the phase-transformation fronts.

The first harmonic phase *phF* now oscillates near the value of 0° on the whole sample surface, with shifts under ±10°, i.e. much smaller than the 180° observed in *Cycle 1*. In both the martensite and transformed austenite zones the oscillations of *phF* also reproduce a pattern which is clearly correlated to the SIMT fishbone-like propagation pattern. This

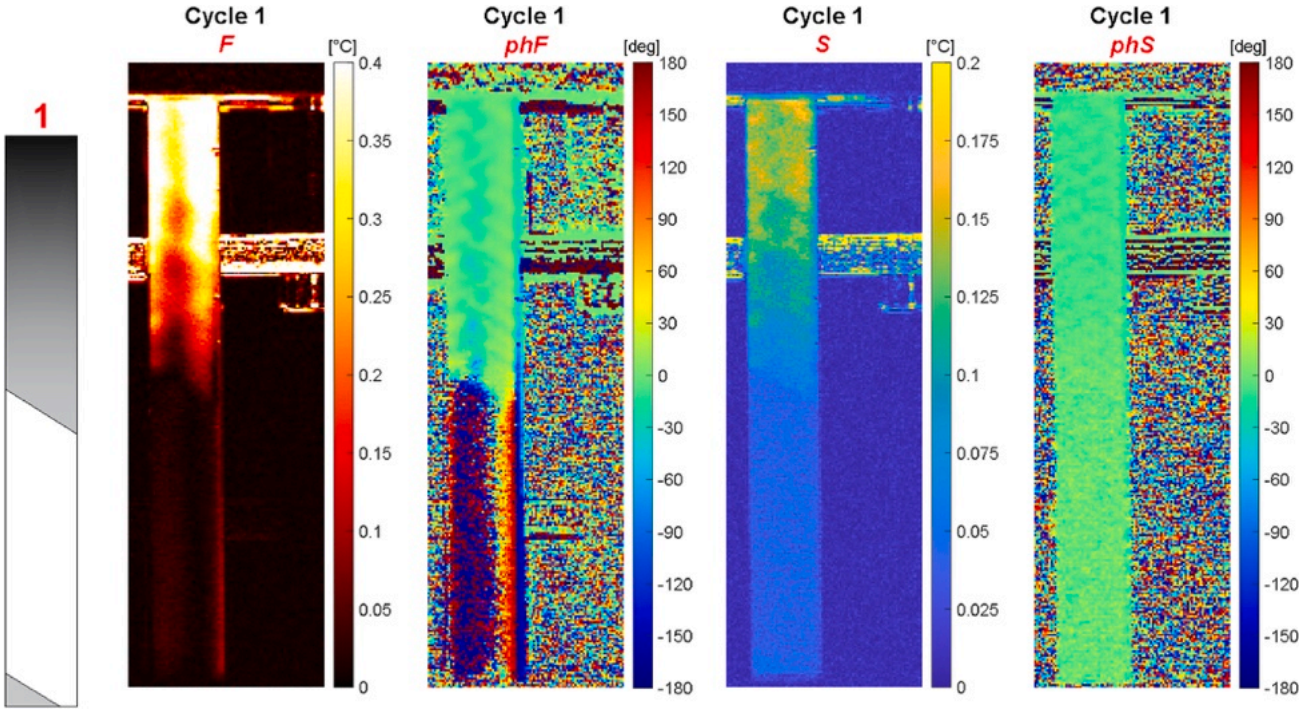

Fig. 9. Amplitude and phase maps of first and second harmonics from *Cycle 1*.

type of propagation was indeed observed in the DIC maps performed on the twin sample S1 (see Fig. 7 b, c, g). The reason why the *phF* map presents little shifts around zero is very likely due to departure from the pure adiabaticity condition. In fact, the formation of localised Lüders bands probably induces inhomogeneities in the material, which alter the thermoelastic response causing internal steep temperature gradients that at low loading frequencies favour the observed phase shifts. In the virgin austenitic region the material status is more homogeneous, and no patterns are obtained in the *phF* map. It is also noticed that the virgin austenite exhibits a zero value of *phF*, contrary to the case of *Cycle 1*. This is due to the load cycle now oscillating at higher stress values than *Cycle 1*. Fig. 12a reports the temperature waveform from ROI DW, which is placed over the virgin austenitic zone. It is still evident how the troughs of the waveform are flattened compared to the peaks. This effect is again attributed to the -cos(2ω) second harmonic, as commented for *Cycle 1*. Contrary to *Cycle 1*, in *Cycle 2* the amplitude of the first harmonic in phase with the load is much stronger and therefore *phF* becomes zero also in the virgin austenite.

Some very interesting features from *Cycle 2* are found in the *S* and *phS* maps. *S* shows higher values in the martensite and transformed austenite as compared to the virgin austenite. By recalling Eq. (6), the differences in *S* would imply a change in the thermoelastic constant $K_{2\omega}$ of the virgin, transformed austenite and martensite, since changes in σ_a among the three zones are not expected to be sufficiently high to explain the observed differences. It is here recalled that the SOTL modelled by Eq. (6) considers a pure uniaxial stress field. As demonstrated by the DIC analysis and further investigated in (Wong et al., 1987), lateral bending moments arise in gripped NiTi tensile samples with localised SIMT. These spurious bending may cause the rise of a biaxial stress field.

The *phS* map shows a 180° shift between the martensitic region on one side, and the transformed and virgin austenitic regions on the other. This significant shift is also found in *Cycle 3* and *Cycle 4* and indicates the *phS* as a very effective parameter to map the austenitic and martensitic zones of the sample. Further studies are needed to correlate the crystal structure to the temperature amplitude and phase maps.

3.4.3. S22: Cycle 3

Cycle 3 is performed after the phase transformation front has further advanced. As shown in the schematic map of Fig. 8, the phase transformation front advances towards the centre of the sample from both the upper and lower sides. As a result, the transformation front becomes the separation between martensite and virgin austenite.

Cycle 3 harmonic maps are reported in Fig. 13. Some features commented from *Cycle 2* are evident also in *Cycle 3*. *F* values are higher for martensite than for virgin austenite. It is observed that *F* and *S* tend to increase in those virgin austenitic regions which most likely anticipate the formation of new brunched Lüders bands, i.e. where the transformation front and the sample edge form an acute angle.

The *phF* map, again, oscillates around 0° over the whole sample surface. By comparing Fig. 12a and b, it is seen that the temperature profiles from ROI UP and ROI DW are very similar between *Cycle 2* and *Cycle 3*, and the same comments made in Section 3.4.2 apply also here. The *phF* map also presents a fishbone pattern in the martensite zone that recalls the brunching transformation fronts.

At the boundary with the virgin austenite, it is now observed that there is a significant negative shift of *phF* of about −20°. This shift implies that the peak of the cosine wave in this region is delayed. The reason for this delay is that there is internal heat transfer in the direction going from the martensitic to the austenitic area, caused by the steep gradients in *F*.

It is meaningful to observe also that the *phS* map again shows a well-distinguished shift of about 180° between the martensitic and the austenitic regions, as already found for *Cycle 2*. Compared to *Cycle 2*, it is immediate to observe how the martensitic area has grown, including now also a little area near the lower grip.

3.4.4. S22: Cycle 4

Cycle 4 is characterised by starting from the lower stress plateau. This means that the reverse phase transformation from martensite to austenite has just begun. Indeed, as shown in Fig. 8, the transformation front is retreating both at the lower grip and at the mid sample length, leaving some martensitic branches.

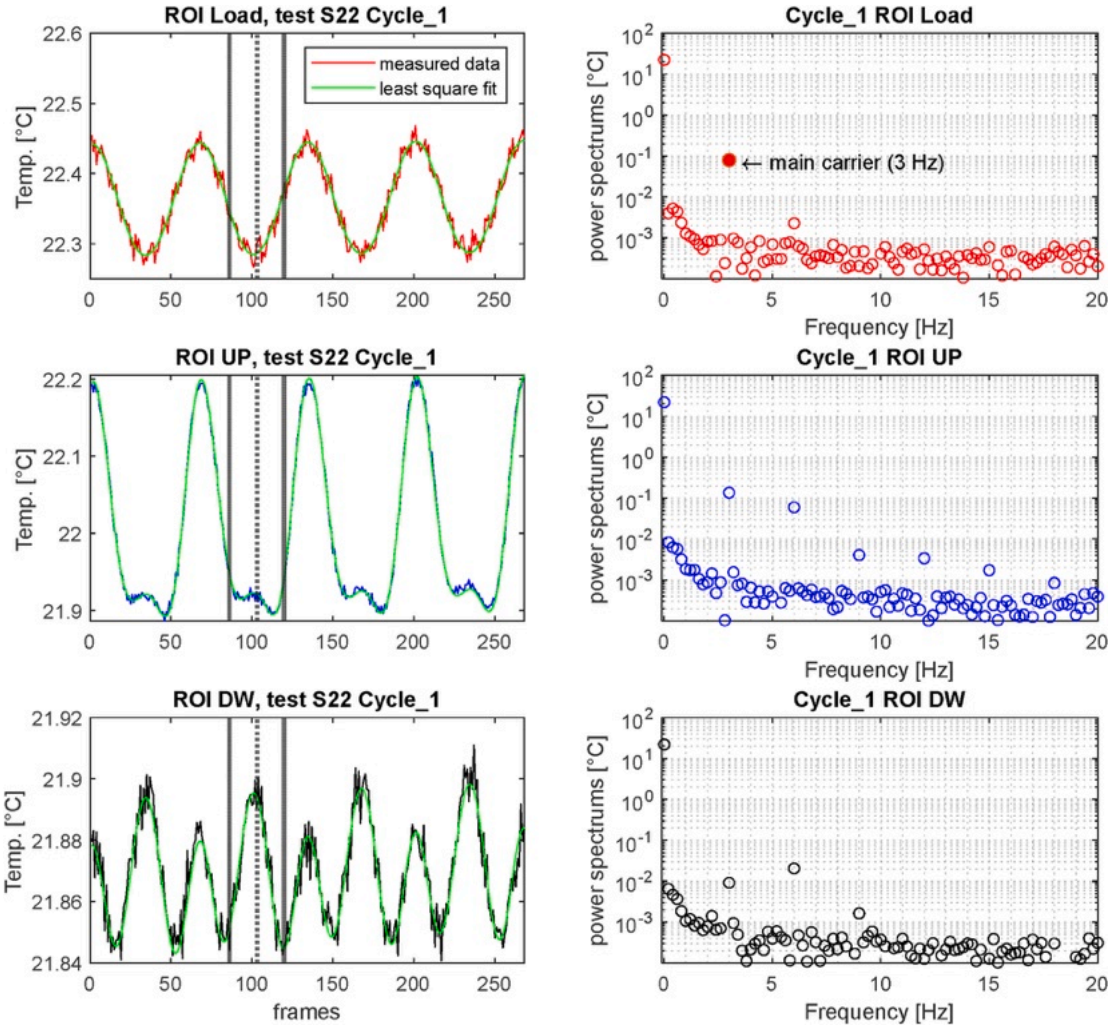

Fig. 10. Average temperature from ROI Load (upper row, first column), ROI UP (central row, first column) and ROI DW (lower row, first column). Experimental curves are superimposed with the curve obtained by least square fitting data with Eq. (1). The second column reports the normalised power spectrums of the measured temperature curves of the first column.

The harmonic maps from *Cycle 4* are shown in Fig. 14, while the temperature profiles from the three reference ROIs are reported in Fig. 12c.

As already observed from *Cycles 2* and *3*, the martensite region exhibits a similar value of F, still significantly higher than the one obtained from the virgin austenite.

The value of *phF* is oscillating around 0° as for *Cycles 2* and *3*. The temperature profile from ROI DW is similar to the previous two cases, as shown in Fig. 12, and therefore considerations made before still apply also for *Cycle 4*. Another similarity with *Cycle 3* regards the higher *phF* shift of −20° observed at the transformation fronts, indicating internal heat flow during cycling from the martensitic to the austenitic region. This marked negative shift may as well be used to identify the transformation fronts. As in the previous cases, the pattern in *phF* in the martensitic region still reveals the fishbone SIMT propagation.

Very remarkable is the confirmation that *phS* is an effective parameter for mapping martensitic and austenitic regions. In fact, it is again found that these regions are characterised by a marked shift of *phS* of about 180°. The shift is very effective also in revealing the martensitic branches that are formed during the retreat of the transformation fronts.

The variations of S in *Cycle 4* also present a further feature. Since the second harmonic experiences a phase jump of 180° passing from a martensitic to an austenitic zone, for this transition to happen smoothly and continuously, the value of S must rapidly go to zero at the transformation front. Indeed, the S map of *Cycle 4* (and to some extent also that from *Cycle 3*) shows zones with very low values of S between austenite and martensite. These are also so concentrated to appear almost as contour lines of the transformation front.

3.5. General discussion

The experimental results described in Section 3.4 show that when NiTi is subject to cyclic sinusoidal loading not involving cyclic phase transformations, its temperature exhibits a peculiar modulation whose waveform carries a strong ω and 2ω harmonic response, where ω is the angular frequency of the loading waveform. This is well shown in Fig. 15, where a comparison is reported about experimental temperature waveforms and two fitting models, one using only one harmonic at ω (Eq. (8)) and the other one using two harmonics at ω and 2ω (Eq. (9)), defined as follows:

$$T(t) = T_o + F\cos(\omega \cdot t + \phi_F) \tag{8}$$

$$T(t) = T_o + F\cos(\omega \cdot t + \phi_F) + S\cos(2\omega \cdot t + \phi_S) \tag{9}$$

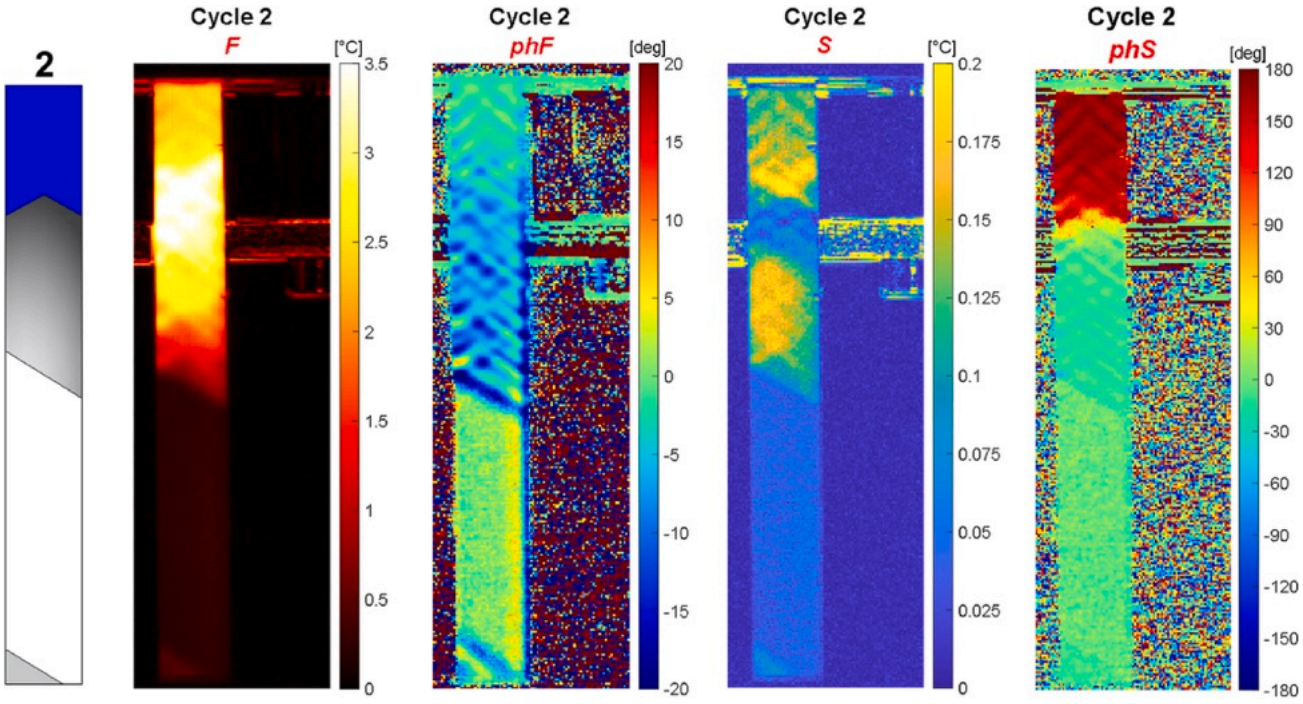

Fig. 11. Amplitude and phase maps of first and second harmonics from *Cycle 2*.

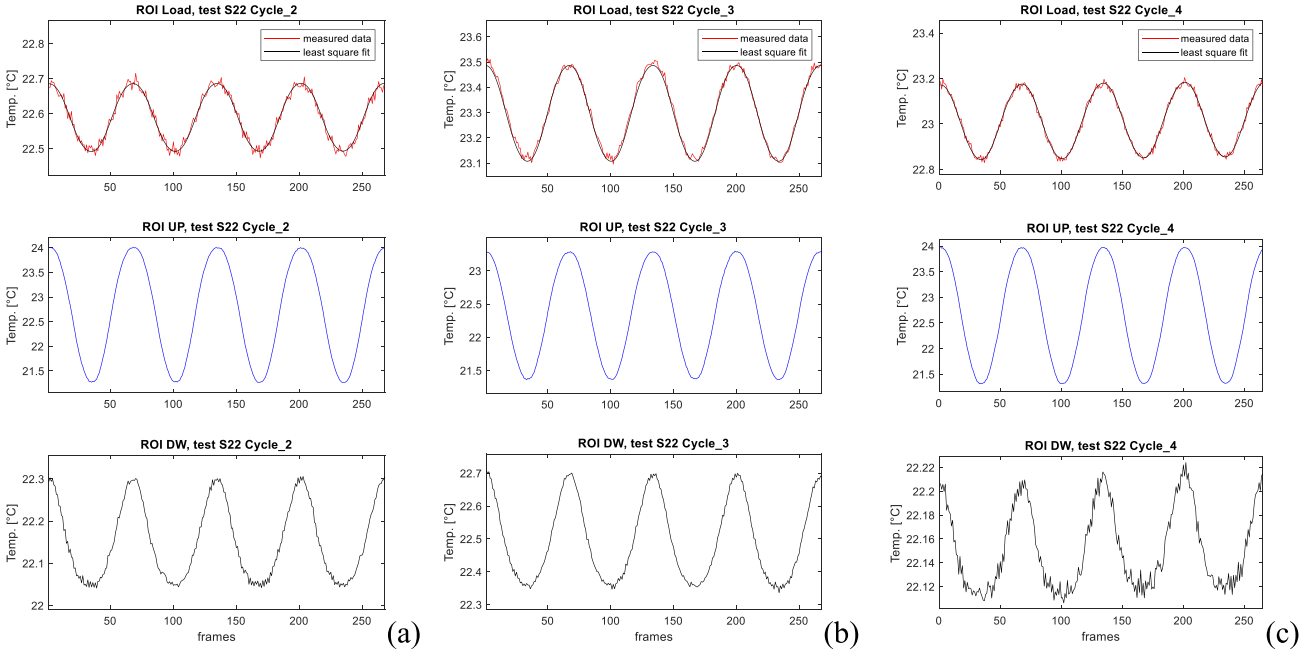

Fig. 12. Average temperature from ROI Load, ROI UP and ROI DW for *Cycles 2*, *3*, *4*. In these loading stages, ROI UP is always over a martensitic zone and ROI DW over a virgin austenitic zone.

It is here remarkable that very few works in the literature have evidenced such marked load-driven modulation of the temperature in NiTi. In general, similar evaluations have been limited to the case where back and forward phase transformations happen within each loading cycle. Clearly, in these cases, the temperature modulation is driven by the eCE.

In this work, the amplitude of cyclic loading is kept under activation of SIMT, i.e. a condition typical of structural fatigue. In this scenario, the main thermomechanical heat source is represented by the TE (Wong et al., 1987; Pitarresi et al., 2020), i.e. the elastic reversible volume change produced by the loads. It is then meaningful to try to correlate the features of the ω and 2ω temperature harmonics with the predictions of the available thermoelastic effect laws, which are recalled in Section 2.5 and that reduce to the FOTL (Eq. (5)) and SOTL (Eq. (6)). Based on

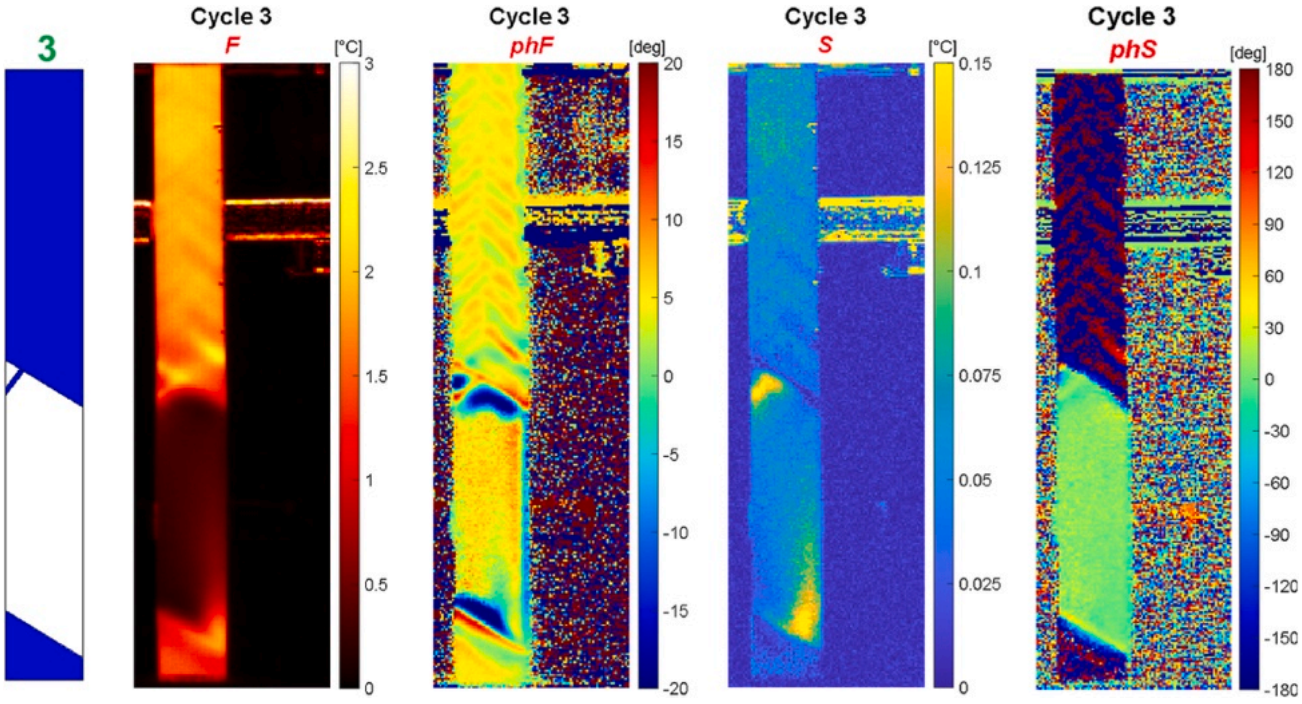

Fig. 13. Amplitude and phase maps of first and second harmonics from *Cycle 3*.

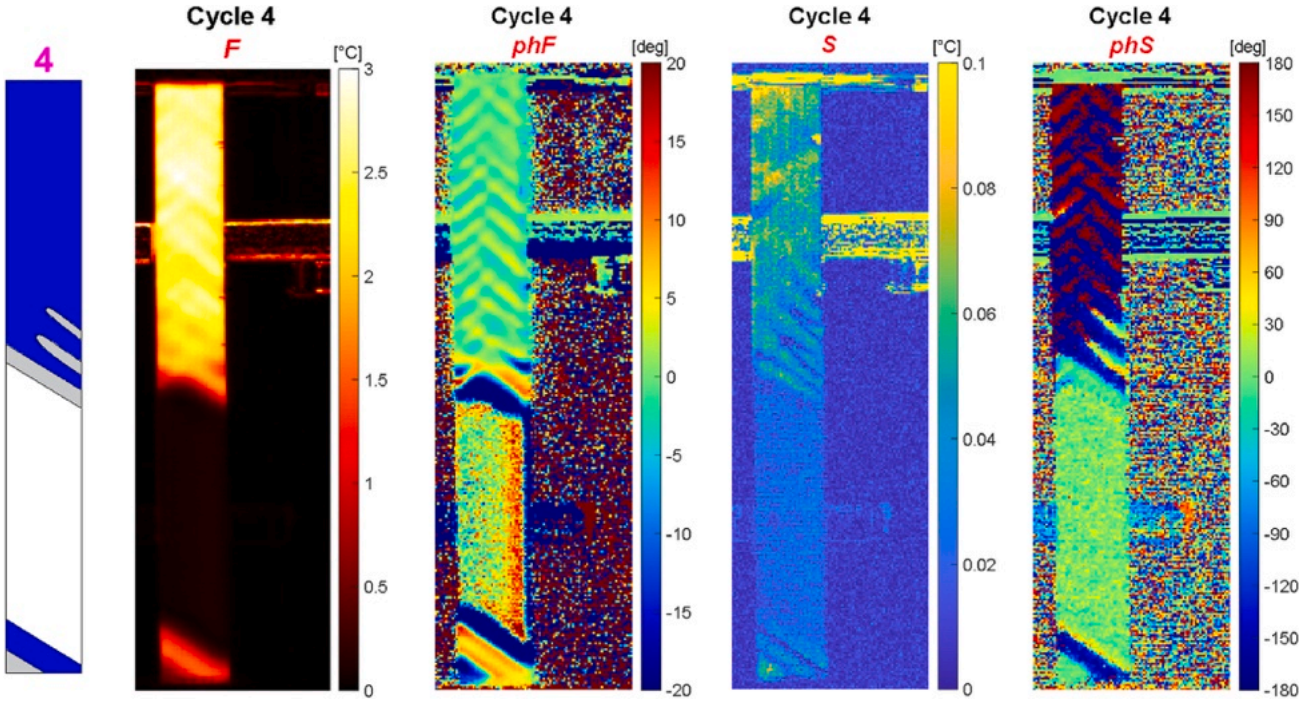

Fig. 14. Amplitude and phase maps of first and second harmonics from *Cycle 4*.

the results reported in Section 3.4, the following findings can be highlighted.

- For all three material status analysed, i.e. virgin austenite, re-transformed austenite and martensite, the temperature first harmonic is generally in phase with the load. This is not predictable with the FOTL, but can be predicted by adopting the SOTL, under the further condition that the derivative of the Young's modulus with the temperature is positive and higher than a certain threshold (see Section 2.5). This result confirms the findings of (Wong et al., 1987; Pitarresi et al., 2020), where the tested sample was a NiTi tube under tension-tension cyclic loading.

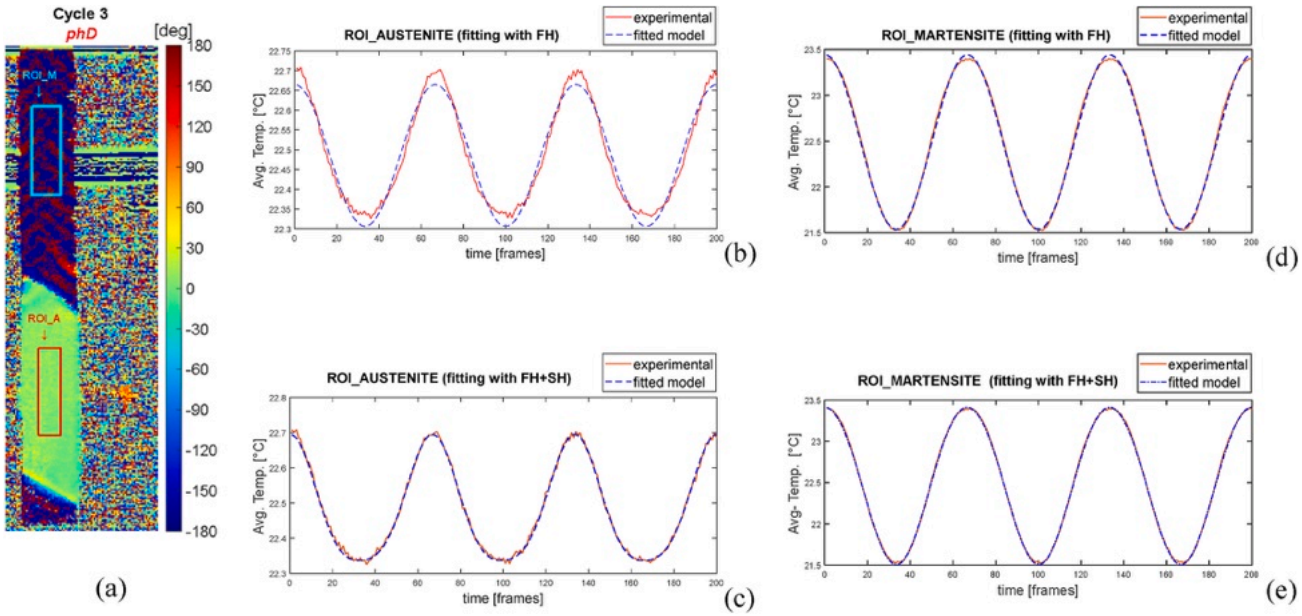

Fig. 15. a) Second harmonic phase map from *Cycle 3* with the definition of ROI_M and ROI_A in the martensite and austenite regions; b, c, d, e) Comparison of experimental average temperature from ROI_M and ROI_A and the fitting models defined by Eq. (8) and Eq. (9).

- The first harmonic amplitude increases quite significantly, and more than linearly, when increasing the average stress σ_m and leaving the stress amplitude $\Delta\sigma_a$ nearly constant. This is, for instance, observed comparing results from *Cycle 1* to *Cycle 2*, with the austenite increasing its first harmonic amplitude by about an order of magnitude. It is also seen that the retransformed austenite exhibits a significantly higher first harmonic response than the virgin austenite, suggesting that changes induced in the material by functional fatigue affect also its intrinsic thermoelastic response.
- The SOTL foresees the presence of a second harmonic with a specific time evolution with respect to the loading wave. This is schematically represented in Fig. 4. In the present work it is found that the austenitic regions satisfy the SOTL prediction on the second harmonic phase (see e.g. Fig. 16a). This is not so for the martensite, which presents a second harmonic phase shifted of 180° with respect to the SOTL prediction (Fig. 16b). While this result is very useful as it allows to map the regions of the sample with either austenite or martensite, the reason why the martensite is in agreement with the SOTL prediction only in relation to the first harmonic and not the second harmonic is not clear, and further testing is required to resolve the mechanism leading to such behaviour.

Considering the above, it is displayed that the available thermoelastic quantitative models given by Eqs. (5) and (6) are not able to fully describe the complex thermomechanical behaviour of NiTi under low-amplitude cyclic loading. It is then not possible, yet, to determine and exploit a robust correlation between stress/strain metrics and thermal parameters, as it is instead viable in conventional Thermoelastic Stress Analysis, when the FOTL can be applied.

4. Conclusions

In the present work, NiTi strips undergoing tensile loading have been monitored with two full-field optical strain and temperature sensing techniques: Digital Image Correlation and Infrared Thermography. Both techniques have helped to monitor the material status during loading/unloading cycles.

Both experimental techniques have been able to identify the occurrence of phase transformation and the formation of localised Lüders bands, and their propagation under sustained straining/unstraining, generating a mesoscale non-homogeneous distribution of austenite and martensite regions.

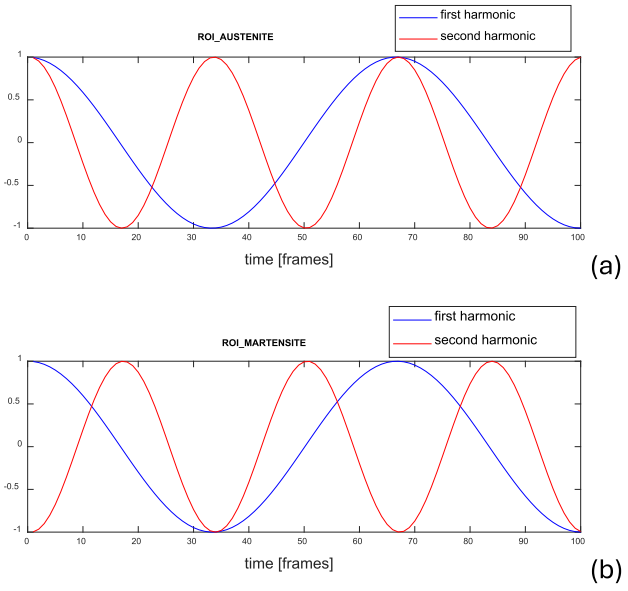

Fig. 16. Normalised plots of temperature first and second harmonic phases from (a) ROI_A and (b) ROI_M, calculated from *Cycle 3* (to be compared with the prediction of Fig. 4).

Several original findings have resulted from the present application of both sensing techniques.

Regarding DIC, it is seen that when separate phase transformation fronts arise, they are generally parallel to each other. Branching is also another favoured propagating mechanism, with the formation of a fishbone-like pattern. By amplifying the transverse strain component obtained from DIC, it is evident that the obliquity of Lüders bands

induces lateral displacements with the rise of bending moments. The pattern in phase transformation fronts is then a natural attempt to reduce such strain energy increase due to the lateral flexural bending.

Regarding IRT, this allowed to acquire temperature during low-amplitude sinusoidal loading below the phase transformation threshold. Such condition resembles that of an in-vivo loading scenario and of structural fatigue loading. The sampled temperature has shown a peculiar waveform with a strong modulation at the angular frequencies of ω and 2ω, where ω is the loading frequency. Maps of the phase and amplitude of the ω and 2ω harmonics have then been retrieved, finding that they show several features that are able to reveal the phase status of the material, as well as providing hints on the transformation history.

The work also reports an attempt to interpret the ω and 2ω harmonics according to the first-order and the second-order analytical laws of the thermoelastic effect, being the latter the main thermomechanical heat source in elastically loaded matter. It is displayed that such quantitative models are not able to fully explain the experimental outcomes. Even so, this work shows that the proposed temperature harmonic analysis still provides qualitative information with potential for the evaluation of NiTi. This approach is even more alluring when considering that it is ideally suited for structural fatigue testing, where other full-field sensing techniques may struggle to achieve a similar richness of output at the same costs. It is here emphasised that the DFT and LSF signal processing used to obtain the harmonics maps can be implemented easily with the help of popular software languages such as *Matlab* or *Python* and require only fractions of seconds to produce results. Therefore, the methodology presented can be considered as a near real-time analysis, which does not require stopping or slowing down the fatigue test, as is often the case with DIC. Moreover, in the perspective of analysing samples with more complex shapes, it is observed that while stereo-DIC would require higher setup and processing times and careful pre-calibrations, the presented IRT methodology remains more straightforward and easier to implement.

CRediT authorship contribution statement

V. Pinto: Writing – original draft, Investigation, Formal analysis, Data curation. **R. Cappello:** Methodology, Investigation, Formal analysis, Conceptualization. **S. Di Leonardo:** Methodology, Formal analysis, Data curation. **G. Catalanotti:** Supervision, Resources, Methodology, Formal analysis. **G. Burriesci:** Supervision, Resources, Methodology, Formal analysis, Conceptualization. **G. Pitarresi:** Writing – review & editing, Supervision, Methodology, Funding acquisition, Formal analysis, Data curation, Conceptualization.

Declaration of competing interest

The authors declare the following financial interests/personal relationships which may be considered as potential competing interests: Valentina Pinto reports financial support was provided by Italian government (PON R&I 2014/2020, S.M. N. 1061 August 10, 2021) as the source of funding for her PhD grant used during this research.

All other authors declare that they have no known competing financial interests or personal relationships that could have appeared to influence the work reported in this paper.

Acknowledgements

The authors gratefully acknowledge the support of Dr. José Eugénio Semedo Garção of the University of Evora (PT) for his precious assistance in setting up and performing tests on sample S2.

The IR thermal camera FLIR X6540sc used in this work has been purchased using funds from the project INTEP PO-FESR 2007/2013 4.1.2.A.

The support by the PON R&I 2014/2020, S.M. N. 1061 August 10, 2021 is acknowledged as the source of funding for the PhD grant of Valentina Pinto.

The support of the grant from the European Union's Framework Program for Research and Innovation - Mission 4 - Component C2 Investment 1.1 (PRIN - 2022) – project title MADforLIFE, code: 2022JE3LRA_001, CUP: B53D23006070006, is also acknowledged regarding the development of the signal processing schemes and algorithms employed in this work.

Appendix B. Supplementary data

Supplementary data to this article can be found online at https://doi.org/10.1016/j.mechmat.2025.105334.

Data availability

Data will be made available on request.

References

Ahadi, A., Kawasaki, T., Harjo, S., Ko, W.-S., Sun, Q., Tsuchiya, K., 2018. Elastocaloric effect at ultra-low temperatures in nanocrystalline shape memory alloys. Acta Mater. https://doi.org/10.1016/j.actamat.2018.11.035.

ASTM F2004-17, 2017. Standard Test Method for Transformation Temperature of Nickel-Titanium Alloys by Thermal Analysis, vol. 13. ASTM International, p. 1. https://doi.org/10.1520/F2004-17.

Blaber, J., Adair, B., Antoniou, A., 2015. Ncorr: open-source 2D digital image correlation Matlab software. Exp. Mech. 55, 1105–1122. https://doi.org/10.1007/s11340-015-0009-1.

Bonsignore, C., Shamini, A., Duerig, T., 2019. The role of parent phase compliance on the fatigue lifetime of Ni–Ti. Shape Memory and Superelasticity 5, 407–414. https://doi.org/10.1007/s40830-019-00253-2.

Boyce, B.R., Lesniak, J.R., 2019. Thermoelastic measurement techniques enabled by self-reference. Conference Proceedings of the Society for Experimental Mechanics Series 7, 125–127. https://doi.org/10.1007/978-3-319-95074-7_24.

Cappello, R., Meneghetti, G., Ricotta, M., Pitarresi, G., 2022. On the correlation of temperature harmonic content with energy dissipation in C45 steel samples under fatigue loading. Mech. Mater. 168. https://doi.org/10.1016/j.mechmat.2022.104271.

Catoor, D., Ma, Z., Kumar, S., 2019. Cyclic response and fatigue failure of Nitinol under tension–tension loading. J. Mater. Res. 34, 3504–3522. https://doi.org/10.1557/jmr.2019.254.

Chrysochoos, A., Huon, V., Jourdan, F., Muracciole, J.M., Peyroux, R., Wattrisse, B., 2010. Use of full-field digital image correlation and infrared thermography measurements for the thermomechanical analysis of material behaviour. Strain 46. https://doi.org/10.1111/j.1475-1305.2009.00635.x.

Churchill, C.B., Shaw, J.A., Iadicola, M.A., 2010. Tips and tricks for characterizing shape memory alloy wire: Part 4 - thermo-mechanical coupling: experimental characterization of active materials series. Exp. Tech. 34, 63–80. https://doi.org/10.1111/j.1747-1567.2010.00619.x.

Delpueyo, C.D., Grédiac, M., Balandraud, X., Badulescu, C., 2011. Studying phase transformation in a shape memory alloy with full-field measurement techniques. In: Optical Measurements, Modeling, and Metrology, pp. 27–32. https://doi.org/10.1007/978-1-4614-0228-2.

Delpueyo, D., Jury, A., Balandraud, X., Grédiac, M., 2021. Applying full-field measurement techniques for the thermomechanical characterization of shape memory alloys: a review and classification. Shape Memory and Superelasticity 7, 462–490. https://doi.org/10.1007/s40830-021-00355-w.

Di Leonardo, S., Cappello, R., Burriesci, G., Pitarresi, G., 2021. Investigation of the thermomechanical response of cyclically loaded niti alloys by means of temperature frequency domain analyses. Materials 14. https://doi.org/10.3390/ma14247866.

Di Leonardo, S., Pitarresi, G., Burriesci, G., 2022. Standard mechanical testing is inadequate for the mechanical characterisation of shape-memory alloys: source of errors and a new corrective approach. Mater. Des. 216. https://doi.org/10.1016/j.matdes.2022.110538.

DigiCamControl web site. https://www.digicamcontrol.com/doc/, 2024.

Dulieu-Barton, J.M., Eaton-Evans, J., Little, E.G., Brown, I.A., 2007. Thermoelastic stress analysis of vascular devices. In: Gdoutos, E.E. (Ed.), Experimental Analysis of Nano and Engineering Materials and Structures. Springer Netherlands, Dordrecht, pp. 5–6.

Dulieu-Barton, J.M., Eaton-Evans, J., Little, E.G., Brown, I.A., 2008. Thermoelastic stress analysis of vascular devices. Strain 44, 102–118. https://doi.org/10.1111/j.1475-1305.2008.00414.x.

Eaton-Evans, J., Dulieu-Barton, J.M., Little, E.G., Brown, I.A., 2006. Thermoelastic studies on Nitinol stents. J. Strain Anal. Eng. Des. 41, 481–495. https://doi.org/10.1243/03093247JSA195.

Furgiuele, F., Magarò, P., Maletta, C., Sgambitterra, E., 2020. Functional and structural fatigue of pseudoelastic NiTi: global vs local thermo-mechanical response. Shape Memory and Superelasticity 6, 242–255. https://doi.org/10.1007/s40830-020-00289-9.

He, Y.J., 2023. Interface propagation and energy dissipation in shape memory alloys. Scr. Mater. 230. https://doi.org/10.1016/j.scriptamat.2023.115420.

Kim, K., Daly, S., 2011. Martensite strain memory in the shape memory alloy nickel-titanium under mechanical cycling. Exp. Mech. 51, 641–652. https://doi.org/10.1007/s11340-010-9435-2.

Launey, M.E., Ong, I., Berg, B.T., Pelton, A.R., 2023. Considerations on tension–tension fatigue predictions for nitinol. Shape Memory and Superelasticity 9, 97–115. https://doi.org/10.1007/s40830-023-00427-z.

Lemaitre, J., Chaboche, J.L., Maji, A.K., 1993. Mechanics of solid materials. J. Eng. Mech. 119. https://doi.org/10.1061/(asce)0733-9399(1993)119:3(642.2.

Mahtabi, M.J., Shamsaei, N., Mitchell, M.R., 2015. Fatigue of Nitinol: the state-of-the-art and ongoing challenges. J. Mech. Behav. Biomed. Mater. 50, 228–254. https://doi.org/10.1016/j.jmbbm.2015.06.010.

Melton, K.N., Mercier, O., 1979. Fatigue of NITI thermoelastic martensites. Acta Metall. 27, 137–144. https://doi.org/10.1016/0001-6160(79)90065-8.

Mitchell, M.R., Berg, B.T., Woods, T.O., Jerina, K.L., 2019. Fourth Symposium on Fatigue and Fracture of Metallic Medical Materials and Devices, vol. 1616. ASTM Special Technical Publication STP. https://doi.org/10.1520/STP1616-EB.

Morgan, N.B., 2004. Medical shape memory alloy applications - the market and its products. Materials Science and Engineering: A 378, 16–23. https://doi.org/10.1016/j.msea.2003.10.326.

Pelton, A.R., Berg, B.T., Saffari, P., Stebner, A.P., Bucsek, A.N., 2022. Pre-strain and mean strain effects on the fatigue behavior of superelastic nitinol medical devices. Shape Memory and Superelasticity 8, 64–84. https://doi.org/10.1007/s40830-022-00377-y.

Petrini, L., Migliavacca, F., 2011. Biomedical applications of shape memory alloys. Journal of Metallurgy 2011, 501483. https://doi.org/10.1155/2011/501483.

Peyroux, R., Chrysochoos, A., Licht, C., Löbel, M., 1998. Thermomechanical couplings and pseudoelasticity of shape memory alloys. Int. J. Eng. Sci. 36. https://doi.org/10.1016/S0020-7225(97)00052-9.

Pieczyska, E., 2010. Activity of stress-induced martensite transformation in TiNi shape memory alloy studied by infrared technique. J. Mod. Opt. 57, 1700–1707. https://doi.org/10.1080/09500341003725748.

Pieczyska, E.A., Tobushi, H., Kulasinski, K., 2013. Development of transformation bands in TiNi SMA for various stress and strain rates studied by a fast and sensitive infrared camera. Smart Mater. Struct. 22. https://doi.org/10.1088/0964-1726/22/3/035007.

Pinto, V., Di Leonardo, S., Galeazzo, M., Burriesci, G., Pitarresi, G., 2024. Temperature harmonic analysis of austenitic niti under dynamic cyclic loading. In: Proceedings of the World Congress on New Technologies. https://doi.org/10.11159/icbb24.112.

Pitarresi, G., Patterson, E.A., 2003. A review of the general theory of thermoelastic stress analysis. J. Strain Anal. Eng. Des. 38, 405–417. https://doi.org/10.1243/03093240360713469.

Pitarresi, G., Cappello, R., Catalanotti, G., 2020. Quantitative thermoelastic stress analysis by means of low-cost setups. Opt Lasers Eng 134, 106158. https://doi.org/10.1016/j.optlaseng.2020.106158.

Reedlunn, B., Daly, S., Hector, L., Zavattieri, P., Shaw, J., 2013. Tips and tricks for characterizing shape memory wire part 5: full-field strain measurement by digital image correlation. Exp. Tech. 37, 62–78. https://doi.org/10.1111/j.1747-1567.2011.00717.x.

Schlosser, P., Favier, D., Louche, H., Orgéas, L., 2009. Experimental characterization of NiTi SMAs thermomechanical behaviour using temperature and strain full-field measurements. Adv. Sci. Technol. 59, 140–149. https://dx.doi.org/10.4028/www.scientific.net/ast.59.140.

Schlun, M., Zipse, A., Dreher, G., Rebelo, N., 2011. Effects of cyclic loading on the uniaxial behavior of nitinol. J. Mater. Eng. Perform. 20, 684–687. https://doi.org/10.1007/s11665-010-9790-2.

Senthilnathan, K., Shamimi, A., Bonsignore, C., Paranjape, H.M., Duerig, T., 2019. Effect of prestrain on the fatigue life of superelastic nitinol. J. Mater. Eng. Perform. 28, 5946–5958.

Soul, H., Yawny, A., 2017. Effect of variable amplitude blocks' ordering on the functional fatigue of superelastic NiTi wires. Shape Memory and Superelasticity 3, 431–442. https://doi.org/10.1007/s40830-017-0126-z.

Technical considerations for non-clinical assessment of medical devices containing nitinol, Guidance for Industry and Food and Drug Administration Staff, 2021. U.S. Department of Health and Human Services Health, Food and Drug Administration Center for Devices and Radiological.

Tušek, J., Žerovnik, A., Čebron, M., Brojan, M., Žužek, B., Engelbrecht, K., Cadelli, A., 2018. Elastocaloric effect vs fatigue life: exploring the durability limits of Ni-Ti plates under pre-strain conditions for elastocaloric cooling. Acta Mater. 150. https://doi.org/10.1016/j.actamat.2018.03.032.

Tzamtzis, S., Viquerat, J., Yap, J., Mullen, M.J., Burriesci, G., 2013. Numerical analysis of the radial force produced by the Medtronic-CoreValve and Edwards-SAPIEN after transcatheter aortic valve implantation (TAVI). Med. Eng. Phys. 35, 125–130. https://doi.org/10.1016/j.medengphy.2012.04.009.

Wadood, A., 2016. Brief overview on nitinol as biomaterial. Adv. Mater. Sci. Eng. 2016. https://doi.org/10.1155/2016/4173138.

Wong, A.K., Jones, R., Sparrow, J.G., 1987. Thermoelastic constant or thermoelastic parameter? J. Phys. Chem. Solid. 48. https://doi.org/10.1016/0022-3697(87)90071-0.

Wong, A.K., Sparrow, J.G., Dunn, S.A., 1988. On the revised theory of the thermoelastic effect. J. Phys. Chem. Solid. 49, 395–400. https://doi.org/10.1016/0022-3697(88)90099-6.

Xiao, Y., Jiang, D., 2022. Effects of structural geometry on the localized deformation of superelastic NiTi sheets. Int J Solids Struct 257. https://doi.org/10.1016/j.ijsolstr.2022.111762.

Xie, X., Kan, Q., Kang, G., Lu, F., Chen, K., 2016. Observation on rate-dependent cyclic transformation domain of super-elastic NiTi shape memory alloy. Mater. Sci. Eng. 671, 32–47. https://doi.org/10.1016/j.msea.2016.06.045.

Yin, H., Li, M., Sun, Q., 2021. Thermomechanical coupling in cyclic phase transition of shape memory material under periodic stressing—experiment and modeling. J Mech Phys Solids, 104199. https://doi.org/10.1016/j.jmps.2020.104199.

Zhang, S., He, Y., 2018. Fatigue resistance of branching phase-transformation fronts in pseudoelastic NiTi polycrystalline strips. Int J Solids Struct 135, 233–244. https://doi.org/10.1016/j.ijsolstr.2017.11.023.

Zhang, Y., You, Y., Moumni, Z., Anlas, G., Zhu, J., Zhang, W., 2017. Experimental and theoretical investigation of the frequency effect on low cycle fatigue of shape memory alloys. Int. J. Plast. 90, 1–30. https://doi.org/10.1016/j.ijplas.2016.11.012.

Zheng, L., He, Y., Moumni, Z., 2016. Effects of Lüders-like bands on NiTi fatigue behaviors. Int J Solids Struct 83, 28–44. https://doi.org/10.1016/j.ijsolstr.2015.12.021.

Zheng, L., He, Y., Moumni, Z., 2017. Investigation on fatigue behaviors of NiTi polycrystalline strips under stress-controlled tension via in-situ macro-band observation. Int. J. Plast. 90, 116–145. https://doi.org/10.1016/j.ijplas.2016.12.008.

Zhu, X., Zhang, X., Qian, M., Wang, Z., Li, A., Chen, Z., Imran, M., Geng, L., 2024. Mesoscopically homogeneous superelastic transformation and related elastocaloric effect in a textured Ti-based shape memory alloy. Intermetallics 164, 108109. https://doi.org/10.1016/j.intermet.2023.108109.